

Gravity wave coupling between the mesosphere and thermosphere over New Zealand

S. M. Smith,¹ S. L. Vadas,² W. J. Baggaley,³ G. Hernandez,⁴ and J. Baumgardner¹

Received 12 December 2012; revised 19 February 2013; accepted 4 April 2013; published 24 May 2013.

[1] All-sky images obtained with the Boston University all-sky imaging system located at the Mount John University Observatory, New Zealand (43.98°S, 170.42°E) show clear evidence of dynamic coupling between the mesosphere and thermosphere. Gravity wave (GW) breaking events in the upper mesosphere at altitudes (z) of 80 to 100 km were observed in the 557.7 nm emission on the evening of 4 March 2009 from 08:40 to 13:50 UT. During this time, unusual oppositely propagating weak northwestward (NW-ward) and strong southeastward (SE-ward) GWs were observed in the all-sky images of the thermospheric atomic oxygen O(¹D) 630.0 nm emission at 250 km altitude. The waves appeared to originate from the same location over New Zealand, with phase fronts nearly parallel to the landmass axis of the South Island of New Zealand. Additionally, the southern portion of the wave train ends abruptly at the southern tip of New Zealand. The SE-ward GWs were stronger and appeared for ~5 h, while the NW-ward GWs were weaker and only appeared for ~1.75 h. We provide evidence that mountain waves were likely generated in the troposphere that evening. Momentum deposition from GW breaking excites secondary GWs. We model these secondary GWs and show that these GWs have a similar morphology and behavior as observed. Wind filtering in the thermosphere can account for the larger amplitudes and persistent appearance of the SE-ward GWs and the smaller amplitudes and less persistent appearance of the NW-ward GWs. Thus, the morphology and behavior of the 630.0 nm GWs suggest that they were secondary GWs generated from mountain wave breaking in the upper mesosphere. We also show that similar SE-ward GWs have occurred in the 630.0 nm emission on other occasions.

Citation: Smith, S. M., S. L. Vadas, W. J. Baggaley, G. Hernandez, and J. Baumgardner (2013), Gravity wave coupling between the mesosphere and thermosphere over New Zealand, *J. Geophys. Res. Space Physics*, 118, 2694–2707, doi:10.1002/jgra.50263.

1. Introduction

[2] The coupling of tidal oscillations between different regions of the lower atmosphere ($z < 110$ km) with the neutral thermosphere ($z > 110$ km) is well documented [e.g., Forbes *et al.*, 2008]. At midlatitudes, the semidiurnal tide is dominant in the mesosphere and lower thermosphere (MLT) and is able to propagate easily through the mesopause into the thermosphere. The diurnal tide is dominant at mid and high altitudes within the thermosphere. High-frequency gravity waves (with periods $T < \text{few hours}$) from the lower atmosphere may propagate to $z = 300\text{--}400$ km before

breaking or dissipating from molecular viscosity and thermal diffusivity [Vadas, 2007; Fritts and Vadas, 2008; Fritts and Lund, 2011]. To reach $z = 200\text{--}300$ km, a gravity wave's (GW's) vertical wavelength λ_z must be large, and its intrinsic phase speed must be larger than $\sim 100 \text{ ms}^{-1}$ [Vadas, 2007]. Additionally, lower frequency GWs can also couple with the upper atmosphere via breaking in the mesosphere in spatially and temporally variable “patches,” which excites high-frequency, large- λ_z secondary GWs [Vadas *et al.*, 2003]. These secondary GWs are created from the larger-scale, deeper deposition of momentum that occurs during breaking; because of their larger λ_z and phase speeds, they can propagate well into the thermosphere prior to dissipating. Medium-scale, fast GWs were observed by Poker Flat incoherent scatter radar (ISR) in Alaska at $z = 180\text{--}250$ km; these waves were subsequently identified as likely being secondary GWs from mountain wave breaking [Vadas and Nicolls, 2009]. Additionally, we note that the dissipation of GWs from viscosity in the thermosphere also excites secondary GWs [Vadas and Liu, 2009, 2013].

[3] Figure 1 shows a map of New Zealand highlighting the 500, 1000, and 1500 m elevation contours.

[4] The New Zealand landmass presents a physical barrier to the prevailing westerly (eastward) winds off the Southern Ocean (particularly during the winter months) and, as a

Additional supporting information may be found in the online version of this article

¹Center for Space Physics, Boston University, Boston, Massachusetts, USA.

²NorthWest Research Associates, Boulder, Colorado, USA.

³Dept. of Physics and Astronomy, University of Canterbury, Christchurch, New Zealand.

⁴Department of Earth and Space Sciences, University of Washington, Seattle, Washington, USA.

Corresponding author: S. M. Smith, Center for Space Physics, Boston University, Boston MA, USA. (smsm@bu.edu)

©2013. American Geophysical Union. All Rights Reserved.
2169-9380/13/10.1002/jgra.50263

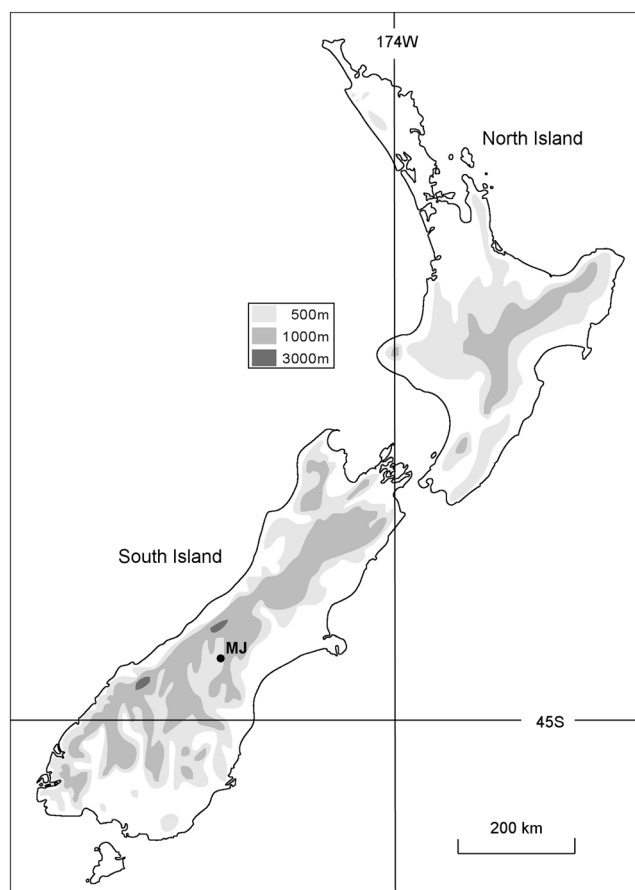


Figure 1. Map of New Zealand highlighting the contours of elevation (A.P. Sturman, personal communication, 2012). The Southern Alps mountain range extends almost along the entire length of the South island and presents a barrier to the prevailing eastward winds. The location of Mt. John Observatory is marked “MJ.”

result, can be a source of orographic GW activity in the lower atmosphere that can then propagate up into the stratosphere and then the mesosphere [Lane *et al.*, 2000; Jiang *et al.*, 2003, 2005; Wu, 2004; Wu *et al.*, 2006]. If the mountains are oriented within a linear chain, then the excited mountain waves are planar. The orientation of the GW fronts recorded in the 630.0 nm images at Mt. John during the night of 4 March 2009 suggests an orographic origin associated with the New Zealand landmass; we show the likelihood of such an origin in this paper although with a several-step coupling process involving different physical processes within different atmospheric regions.

[5] Here, we report on a dynamically active night in the mesosphere and thermosphere in which GW activity was observed over a very wide altitude region. In particular, oppositely propagating GWs with approximately linear phase fronts were recorded in the 630.0 nm nightglow at $z=250$ km by the Boston University all-sky imager at Mount John University Observatory (MJUO) during a period of strong GW activity occurring in the mesosphere (below 100 km). We use modeling to show that these GWs were likely secondary GWs generated by the breaking of mountain waves from wind flow over the New Zealand landmass in a two-step coupling process.

2. Instrumentation

[6] The Boston University all-sky imager has been operating at the Mount John Observatory, New Zealand (43.98°S , 170.42°E), since February 2009. The instrument utilizes an Andor 2048×2048 $13.6 \mu\text{m}$ -pixel bare-CCD detector cooled to $< -50^{\circ}\text{C}$ with a resulting quantum efficiency of $\sim 95\%$ in the visible region. Three upper-mesospheric emissions are recorded: OH broadband IR emission (695–1050 nm), Na (589.0–589.6 nm) and $\text{O}^{\text{I}}\text{S}$ (557.7 nm), and one thermospheric emission: $\text{O}^{\text{I}}\text{D}$ (630.0 nm) from ~ 250 km. An off-band filter (572.9 nm) is also used for calibration purposes. Observations consist of each filter being cycled sequentially throughout each night. The integration time was 120 s, except for 30 s for the OH images. The cycle time for each filter during this night was almost 9.5 min.

[7] Reduction of the raw all-sky images was performed using our standard procedures [Smith *et al.*, 2009], initial bias, and dark subtraction followed by flat-fielding to remove effects due to vignetting, van Rhijn brightening, atmospheric absorption, and the narrowband filter characteristics. The removal of stars and the Milky Way was then undertaken and the images calibrated photometrically into Rayleigh brightness units. Finally, the images were mapped onto the Earth’s surface using the nominal emission layer heights—a process called unwarping.

3. Observations and Results

3.1. Thermospheric Gravity Wave Activity

[8] Thermospheric GWs were recorded in the 630.0 nm nightglow emission over Mt. John Observatory on the evening of 4 March 2009 (see Figure 2). These six unwarped all-sky images were processed using a high-frequency pass (HFP) filter which retains the small-scale gravity wave structures. Because the images were also calibrated into Rayleigh brightness units, the HFP-filtered images are normalized to 1.0 which also makes the determination of wave amplitudes a relatively simple matter.

[9] The SE-ward waves exhibited larger amplitudes than the NW-ward waves. They propagated with an observed horizontal phase speed of $c_{\text{obs}} = 104 \text{ ms}^{-1}$ at an azimuth heading of 158° (clockwise from North) and with a mean horizontal wavelength of $\lambda_x = 255$ km. The NW-ward waves were significantly weaker and exhibited a smaller mean horizontal wavelength of $\lambda_x = 84$ km and a larger observed horizontal phase speed of $c_{\text{obs}} = 177 \text{ ms}^{-1}$. The measured parameters and behavior associated with the waves shown in Figure 2 are listed in Table 1. Animations of the 630.0 nm and 557.7 nm wave events during the night can be viewed in the supporting information.

[10] Comparing Figures 1 and 2, we can see that the wave phase lines (fronts) were nearly parallel to the mountainous axis of the New Zealand landmass. In particular, the waves were approximately parallel to the axis of 1000 m elevation contour in New Zealand.

[11] The 630.0 nm activity was unusual for a number of reasons. Firstly, it consisted of two extensive and simultaneous GW trains that propagated in opposite directions, one southeastward (SE-ward) and the other northwestward (NW-ward). The waves were aligned from SW to NE with an azimuth of $68^{\circ} \pm 5^{\circ}$. The SE-ward GWs were stronger

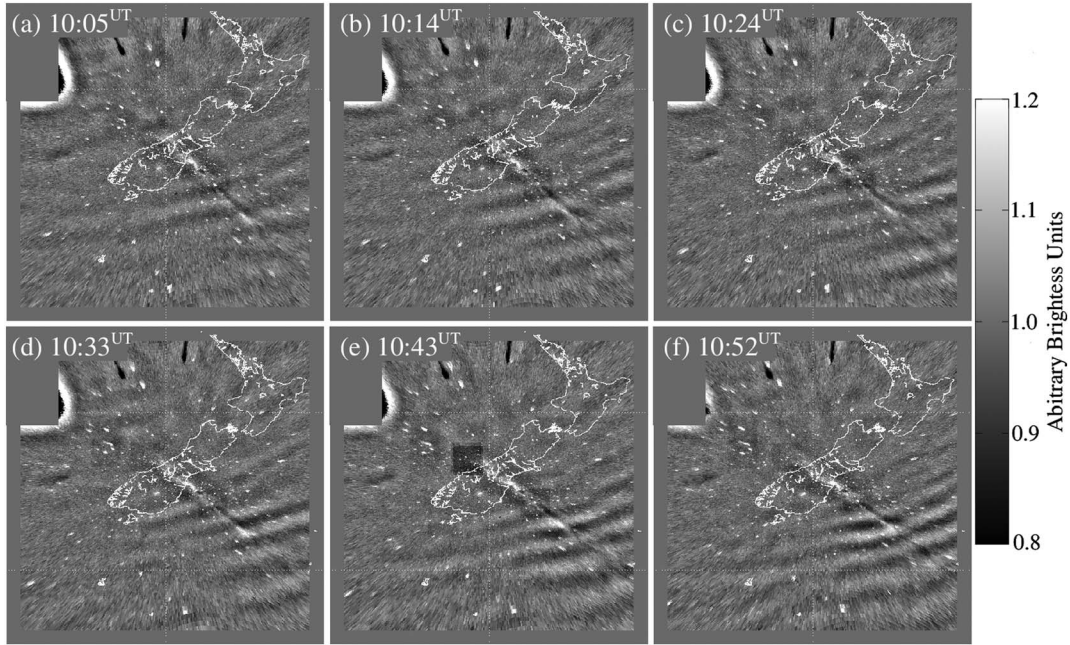


Figure 2. A series of unwarped, HFP-filtered (see text), 630.0 nm all-sky images from MJUO on 4 March 2009 showing the pair of gravity wave events over New Zealand. Two sets of propagating waves are evident in the images: a strong SE-ward set and a weak NW-ward set. Both sets appear to be aligned closely with, and originate from, the mountainous axis of the South Island of New Zealand. Note that the bright feature aligned NW-SE is the Milky Way. North is at the top and east is to the right.

and appeared for ~ 5 h, from 08:40 to 13:50 UT. The NW GWs were weaker and only appeared for ~ 1.75 h, from 9:10 to 10:50 UT. Secondly, the waves appear to originate from an extended linear region, as opposed to a localized point (see section 4), which is roughly aligned with and situated directly over the landmass of New Zealand. The closest point to Mt John Observatory that the SE-ward 630.0 nm waves first began to appear was at 190 ± 35 km to the southeast.

[12] Additionally, the southern portions of the SE-ward wave train (in a coordinate system perpendicular to the wave propagation direction) end abruptly to the south and west of the landmass. The northeastern portion of the wave trains extended out of the field of view. Both the alignment of the wavefronts and the southern end of the wave trains strongly suggest that the origin of the thermospheric GWs was associated with the landmass of New Zealand in some way.

[13] Furthermore, the pair of wave events, propagating in opposite directions, originated simultaneously from the

same region of space within the field of view of the imager, which strongly suggests a common generation mechanism and origin.

[14] We investigate the possibility of OH contamination in the 630.0 nm images during the night of 4 March 2009. The OH Meinel bands occur across a wide spectral region, beginning faintly near 510 nm and increasing in brightness with increasing wavelength until ending near 2300 nm in the far infrared. Mesospheric OH emission contamination within the passband of narrowband filters, such as at 630.0 nm, is well known [e.g., *Hernandez, 1974; Burnside et al., 1977*] and is a phenomenon familiar to the authors (S.M.S., G.H., and J.L.B.). The 630.0 nm O(¹D) line is located at 630.0304 nm [*Osterbrock et al., 1996*]. Three spectral lines from the OH(9–3) band lie within the bandwidth of the Boston University (BU) imager’s 630.0 nm filter at MJUO: the P₂(3) line at 629.7903 nm and the P₁(3) doublet at 630.6869 and 630.6981 nm [*Hernandez, 1974; Burnside et al., 1977*]. The P₁(2) line at 628.7434 nm lies near the blue-ward edge of the filter band pass also.

Table 1. The Observed Wave Parameters Associated With the 630.0 nm and MLT Waves^a

Emission	Azimuth ($\pm 2^\circ$)	c_{obs} (ms ⁻¹)	λ_{obs} (km)	T _{obs} (min)	T _{int} (min)	λ_z (km)	c_{IH} (ms ⁻¹)	c_{gz} (ms ⁻¹)	c_{gH} (ms ⁻¹)
<i>Thermospheric Gravity-Wave Activity</i>									
O(¹ D) 250 km	158 (SE)	104.1 (17.7)	254.8 (55.7)	42.7 (10.1)	30	88	139	40	126
O(¹ D) 250 km	338 (NW)	177.0 (17.2)	83.6 (16.7)	7.9 (1.4)	10	340	136	29	18
<i>Mesospheric Gravity-wave Activity</i>									
O(¹ S) 97 km	160–180	50.4 (5.8)	106.8 (36.7)	35.8 (12.7)	–	–	–	–	–
Na 92 km	160–180	49.5 (5.9)	88.6 (29.0)	30.0 (10.0)	–	–	–	–	–
OH 85 km	160–180	49.4 (6.2)	106.8 (26.8)	36.5 (10.0)	–	–	–	–	–

^aThe sample standard deviations of the means are shown in parentheses. The intrinsic parameters for the thermospheric GWs are calculated using the mean values with an assumed 40 ms⁻¹ NW-ward wind.

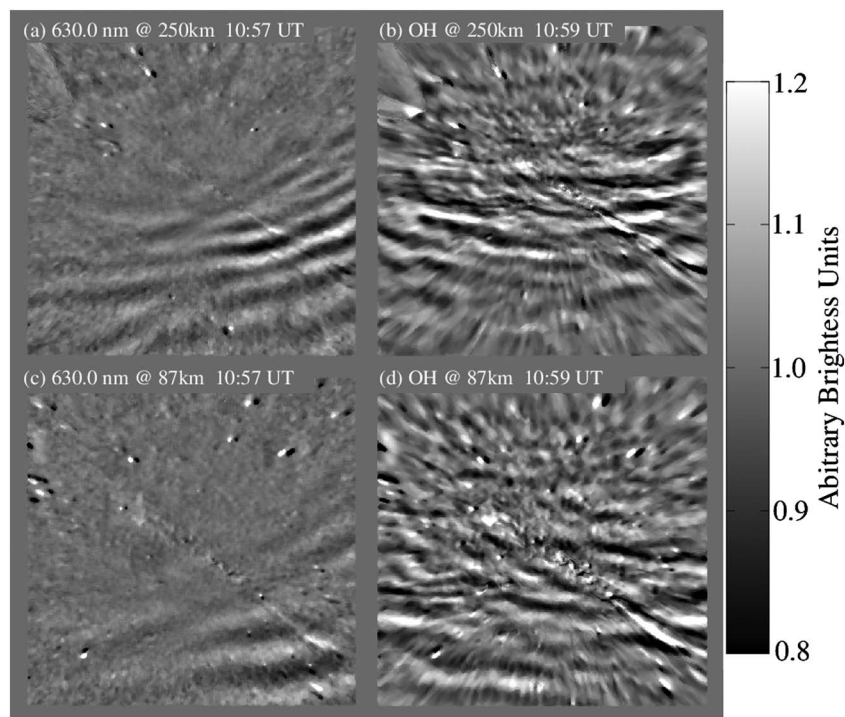


Figure 3. (a–d) Four unwarped time-difference 630.0 nm and OH images obtained during the time when the largest wave amplitudes were exhibited in the 630.0 nm images (~11:00 UT). Figures 3a and 3b were unwarped to an altitude of 250 km and Figures 3c and 3d to 87 km. The images indicate that negligible OH contamination occurred within the 630.0 nm images and that the 630.0 nm wave signatures were thermospheric in origin.

[15] The 630.0 nm filter used at MJUO is a 105 mm diameter, narrowband interference filter with a central wavelength of 630.124 nm, a maximum transmission of 72.3%, and a full-width at half-maximum (FWHM) spectral width of 1.623 nm. The nominal line brightness of the $P_1(3)$, $P_2(3)$, and $P_1(2)$ lines at midlatitudes are 5–8 R, 2–4 R, and 4–6 R, respectively [Hernandez, 1974; Burnside *et al.*, 1977], which is near the detection threshold of the imaging system. Hence, typically, the level of OH contamination in the 630.0 nm images is expected to be small. However, on occasion, the mesospheric OH radiance may be enhanced by a factor of two or more and result in contamination within the filter band passes of several commonly studied nightglow emissions (e.g., 630.0 nm). The contamination manifests as faint waves superimposed on the recorded thermospheric activity. It can also become an issue when the 630.0 nm emission is low due to factors such as low solar activity.

[16] The 630.0 nm and OH filter positions are adjacent in the nightly cyclic observing sequence and are separated in time by 129 s (the time required to acquire a 630.0 nm image). Figure 3 shows pairs of time-difference (TD) images obtained with the 630.0 nm and OH filters, respectively. TD images are the resulting difference of two subsequent images. Variations within the original images are retained, whereas stationary structures are removed. The time stamps of the 630.0 nm images used were 10:52:04 UT and 11:01:31 UT (10:57 UT) and, for the OH images, 10:54:15 UT and 11:03:41 UT (10:59 UT). This time period was chosen because the 630.0 nm wave amplitudes were greatest, and so, if it was due to OH contamination, the OH images should exhibit exactly the same wave

morphologies and structures. The OH and 630.0 nm images have both been unwarped to 87 km (Figures 3a and 3b) and 250 km (Figures 3c and 3d). The high level of mesospheric gravity wave activity that occurred in the OH emission during the night is clearly evident and featured a particularly extensive wave event propagating southward. In contrast, the 630.0 nm images show a localized set of waves in the southeastern quadrant that are propagating toward the southeast. In addition, the 87 km 630.0 nm images show larger-scale waves compared to those in the 87 km OH images.

[17] Gravity wave parameters were deduced from unwarped images of the four emissions: OH, Na, $O(^1S)$, and $O(^1D)$. The thermospheric $O(^1D)$ parameters (from 250 km) showed distinct differences compared to those of the three mesospheric emissions. In addition, the 87 km 630.0 nm wave parameters were compared to the 87 km OH parameters. The parameters are presented in Figure 4 as the relationship of the horizontal wavelength as a function of the observed period for all the wave events imaged during the night of 4 March 2009. Also shown in Figure 4 are wave parameters deduced from the 630.0 nm images that were unwarped to 87 km altitude in order to test for any possible mesospheric OH contamination in the 630.0 nm images. The 87 km 630.0 nm wave parameters (open triangles) show a clearly different relationship to the parameters derived from the OH filter (filled triangles) as well as the other mesospheric emissions. The range of the scale sizes and wave period are also both significantly reduced. The thermospheric waves (250 km 630.0 nm) in Figure 4 clearly exhibit larger observed phase speeds, as represented by the fitted slopes. Additionally, there is also a marked difference between

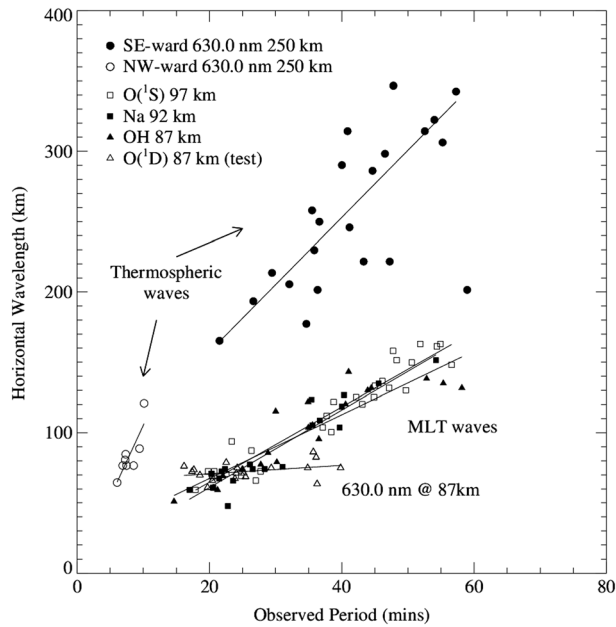


Figure 4. Plot of horizontal wavelength as a function of the observed wave period for the waves observed during the night of 4 March 2009. The MLT and thermospheric waves show distinct differences. Wave parameters obtained from the 630.0 nm images unwrapped to 87 km, as a test for OH contamination (open triangles), show a distinctly different relationship compared to the OH images (filled triangles).

the thermospheric waves, with the NW-ward waves having larger observed phase speeds than the SE-ward waves. Hence, we can be confident that the emission modulation recorded in the (250 km) 630.0 nm images was occurring in the thermosphere.

[18] All of the filters used were calibrated to ~ 0.05 nm resolution using our in-house MacPherson spectrophotometer and the solar spectrum as a standard line source. The rejection factor outside the band pass of the narrowband filters (630.0 nm included) and into the IR was typically 10^5 – 10^6 . Most important, however, was that the OH filter used in this present study (RG-695) has a broad transmission window of 100% starting at ~ 700 nm through to ~ 1000 nm, where the quantum efficiency (QE) of the CCD camera finally decreases to zero. Hence, any IR leakage into the narrowband filters would have been much more evident in the OH filter images. The 630.0 nm waves were not visible at all in the OH images, and so we can be certain that the 630.0 nm waves were not due to mesospheric OH emission.

[19] Figure 5 shows the measured zenith radiance of the four emissions and the off-band filter during the course of the night. The 630.0 nm zenith brightness was correlated with the passage of the SE-ward 630.0 nm waves. From 9:45 to 10:30 UT, the mean 630.0 nm emission level increased by 75% from 150 ± 4 R to a maximum brightness of 206 ± 6 R just after 10:30 UT. The emission then decreased to initial levels at 12:00 UT. The 630.0 nm zenith brightness was also correlated with the brightness amplitude of the SE-ward waves. The waves exhibited brightness amplitudes of 4–12 R (2–5%) above the mean background level and were largest at about 10:50–11:00 UT. Notice that

the OH, Na, and 572.9 nm (off-band) emissions show a general decline during the course of the night with very little correlation with the 557.7 and 630.0 nm emissions—another indication that there was little mesospheric OH contamination in the 630.0 nm images.

[20] One other possibility was that the 630.0 nm waves were due to emission contamination from a neutral metal layer, such as FeO. This emission originates from the upper mesosphere [Evans *et al.*, 2010; Saran *et al.*, 2011] and is a spectrally broad pseudo-continuum emission occurring between 540 and 68 nm. It therefore encompasses the bandwidths of the 557.7 nm, 589.0–6 nm, and 630.0 nm filters. One of the authors (S.M.S) has observed this type of emission in Na all-sky images on previous occasions; however, there is no evidence of FeO emission during this present night.

[21] From these analyses, we can conclude that (1) there was no evidence of OH contamination in the 630.0 nm images during the night of 4 March 2009, (2) any level of contamination that was present was negligible, and (3) the observed 630.0 nm wave signatures were thermospheric in origin.

[22] The waves seen in Figure 2 were quite unlike the medium-scale traveling ionospheric disturbances (MSTIDs) usually seen in 630.0 nm all-sky imagery which tend to exhibit large broad quasi-wavelike features that propagate across the sky [e.g., Kelley and Makela, 2001; Saito *et al.*, 2002; Shiokawa *et al.*, 2003; Martinis *et al.*, 2010]. The waves reported here were well-defined wave structures that appeared quasi-monochromatic in a way similar to those observed frequently in the nighttime mesospheric emissions of OH, Na, and O(¹S), nominally at 80–100 km in altitude.

[23] The 630.0 nm emission lifetime is 110 s; however, when other mechanisms become important, such as quenching, the apparent lifetime decreases. Hernandez [1972] measured an effective 630.0 nm emission lifetime of 20 s. In that case, with a phase speed of 104 ms^{-1} (see Table 1), the 630.0 nm waves would traverse 0.5° field of view or 2.1 km in horizontal distance at 250 km altitude. The O(¹D) layer is ~ 50 km (FWHM), which is slightly smaller

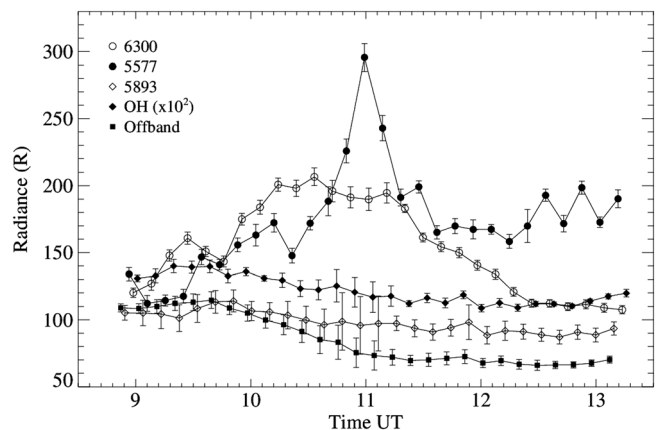


Figure 5. Calibrated zenith brightness measurements of the four emissions at Mt. John Observatory during the night of 4 March 2009. The OH radiance has been reduced by a factor of 100 for comparison purposes.

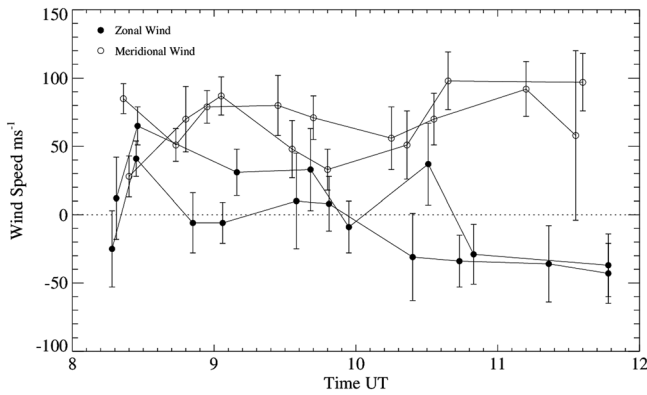


Figure 6. Plots of neutral zonal and meridional 630.0 nm winds obtained by FPS measurements during the nights of 7 and 8 March 1996 at Mt. John.

(~ 0.7) than a scale height at that altitude. To be recorded, gravity waves would therefore require a vertical wavelength greater than the layer thickness. Large λ_z waves have propagation speeds slower than the effective $O(^1D)$ emission lifetime of ~ 20 s so the wave patterns would have relatively sharp edges, although not as sharp as in those for waves in the mesosphere. Diffusion would also be a factor in causing some decrease in the sharpness of the 630.0 nm waves [Hays and Atreya, 1971]. The OH emission lifetime is ~ 10 ms, which is much smaller than the wave period. As a comparison, the BU imager's resolution of 1 pixel width at zenith corresponds to 0.3° or 1.2 km at 250 km altitude.

[24] No thermospheric winds were available during the time of the wave event. However, the midlatitude diurnal tide wind field in the thermosphere is thought to be relatively stable from day to day throughout the year. The diurnal tide is considered to be the most important tidal component of the neutral wind at $z=250$ km. In Figure 6, we examine the neutral zonal and meridional wind measured on 7 and 8 March 1996 with the high-resolution Fabry-Perot spectrometer (FPS) collocated at Mt. John. This is the closest year to the time of the wave event under study. A consistent northwestward wind flow is seen during the 8:00–11:00 UT time period. At $\sim 10:00$ UT, the zonal wind is negligible, and the meridional wind is northward and reaches a local

minimum of $\sim 40\text{--}70$ ms^{-1} . Figure 7 shows the results from the high-resolution thermosphere-ionosphere-mesosphere-electrodynamics general circulation model (TIME-GCM) [Roble and Ridley, 1994]. The diurnal tide is seen to be the largest contributor to the wind at this altitude. The meridional wind increases from 8:00 to 12:00 UT, similar to Figure 6, and is negligible at $\sim 9:00$ UT. In contrast, the zonal wind decreases from 8:00 to 12:00 UT, although with a magnitude which is much larger than that shown in Figure 6. At 10:00 UT, the zonal wind is negligible, and the meridional wind is 50 ms^{-1} . Both the 1996 FPS winds and the TIME-GCM indicate that the neutral winds at $z=250$ km were NW-ward at $\sim 10:00$ UT on 4 March 2009, with a magnitude of 50 ms^{-1} . Therefore, we conclude that the observed SE-ward (NW-ward) waves propagated against (with) the local wind at 10:00 UT. This caused the SE-ward waves to have larger vertical wavelengths λ_z and intrinsic phase speeds c_{IH} than at lower altitudes, which enabled them to propagate deeper into the thermosphere prior to dissipating [Vadas, 2007; Fritts and Vadas, 2008]. We also conclude that the NW-ward waves had smaller vertical wavelengths and intrinsic frequencies in the northward wind, which caused them to dissipate at lower altitudes within the thermosphere. If a wave dissipates below $z=220$ km, then it is unlikely to be detected as a fluctuation in the 630.0 nm emission.

[25] We now estimate the intrinsic GW parameters. The intrinsic frequency is given by $\omega_{\text{int}} = \omega_{\text{obs}} - k_H U_H$, where ω_{obs} is the observed wave frequency in rad s^{-1} , respectively, $k_H = 2\pi/\lambda_{\text{obs}}$ is the wavenumber along the direction of propagation, λ_{obs} is the horizontal wavelength, and U_H is the wind speed along the direction of wave propagation. From Figures 6 and 7, we assume the background wind is $U_H = 40$ ms^{-1} toward the northwest at $\sim 10:00$ UT. Then, $U_H = -40$ ms^{-1} for the SE-ward waves, and $U_H = 40$ ms^{-1} for the NW-ward waves. Then the estimated intrinsic periods of the NW and SE-ward waves are 10 and 30 min, respectively. The TIME-GCM suggests a neutral temperature of 740 K and a buoyancy period of 10–11 min at $z=250$ km and 10:00 UT. Therefore, the NW-ward GWs likely had intrinsic periods quite close to the buoyancy period, which implies that they were quite close to evanescence (reflecting downward). Ray tracing suggests that GWs with intrinsic periods quite close to the buoyancy period may

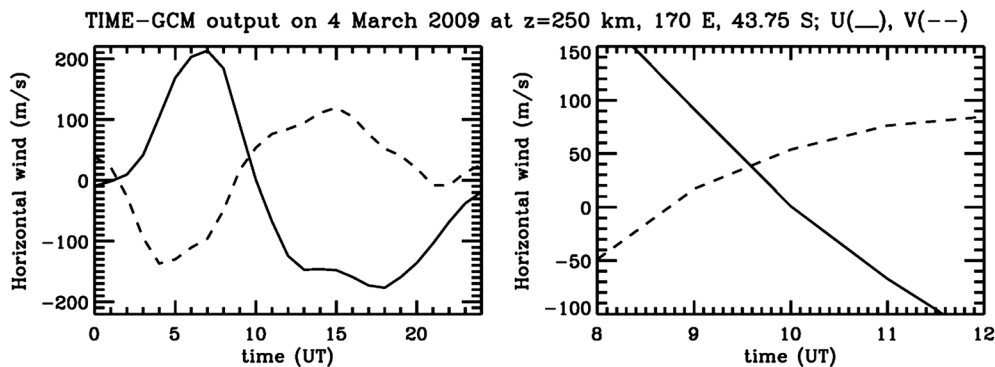


Figure 7. Neutral zonal (solid) and meridional (dashed) winds at $z=250$ km, 170°E , and 43.75°S from the TIME-GCM on 4 March 2009 (left panel). A blowup for the time of interest is shown in the right panel.

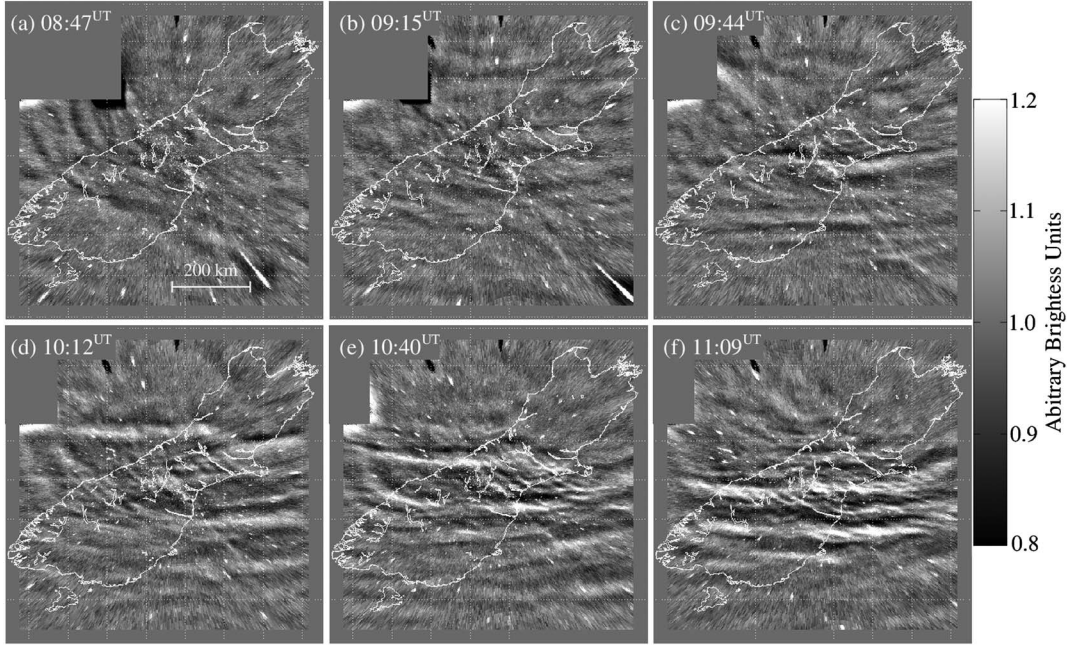


Figure 8. A series of unwarped all-sky images showing the gravity wave activity in the 557.7 nm emission from near 97 km altitude on the night of 4 March 2009. The marked nonsinusoidal and surge-like appearance of the waves and the presence of the small-scale ripples, the result of local instabilities, indicate that wave breaking is occurring. Similar behavior and scale sizes were seen in the OH and Na images during the same period. North is to the top, and east is to the right.

propagate high into the thermosphere prior to dissipating because of their large vertical wavelengths λ_z [Vadas, 2007]. We use the anelastic dispersion relation to estimate the GW vertical wavelengths, λ_z [Fritts and Alexander, 2003]:

$$m^2 = (k_H N / \omega_{\text{int}})^2 - k_H^2 - 1 / (4 H^2), \quad (1)$$

where $m = 2\pi / \lambda_z$. From the TIME-GCM, the Brunt-Vaisala frequency, N , is 0.011 rad s^{-1} , and the density scale height is $H = 22 \text{ km}$ at 250 km and 10:00 UT. For the NW and SE-ward GWs, we find that $\lambda_z = 340$ and 88 km , respectively. This corresponds to similar intrinsic horizontal phase speeds, $c_{\text{IH}} = \omega_{\text{int}} / k_H$, of $c_{\text{IH}} = 136$ and 139 ms^{-1} , respectively. According to Vadas [2007], these speeds are fast enough to ensure that the GWs have their maximum amplitudes at an altitude (dubbed z_{diss}) above 225 km. Note that above z_{diss} , a GW's amplitude decays rapidly with altitude due to molecular viscosity.

[26] We now calculate the intrinsic horizontal and vertical group velocities, $c_{\text{gH}} = \partial \omega_{\text{int}} / \partial k_H$ and $c_{\text{gz}} = \partial \omega_{\text{int}} / \partial m$, respectively. For the SE-ward waves, we find that $c_{\text{gH}} = 126 \text{ ms}^{-1}$ and $c_{\text{gz}} = 40 \text{ ms}^{-1}$ with a corresponding propagation angle of 17° to the horizontal. In comparison, for the NW-ward waves, we find that $c_{\text{gH}} = 18 \text{ ms}^{-1}$ and $c_{\text{gz}} = 29 \text{ ms}^{-1}$, indicating a more vertical propagation angle (58° to the horizontal). Note that both GWs have similar intrinsic phase speeds.

[27] Let us now understand how the intrinsic quantities of these GWs vary with the background wind. First, we examine the case where the wind along the propagation direction is zero, $U_H = 0$ (as it might have been at 9:00 UT from Figure 7). Then, the SE-ward GWs would have $\lambda_z = 60 \text{ km}$ and $c_{\text{IH}} = 100 \text{ ms}^{-1}$; this smaller phase speed would

have resulted in more dissipation (and therefore smaller amplitudes) within the 630.0 nm layer [Vadas, 2007], whereas the NW-ward GWs would not have reached this altitude, because $m^2 < 0$ (i.e., these GWs would have reflected downward at a lower altitude). Next, we examine the case where the background wind was instead $U_H = 100 \text{ ms}^{-1}$ to the northwest (as it may have been at 12:00 UT from Figure 7). Then the SE-ward GWs would have intrinsic periods of 21 min, $\lambda_z = 144 \text{ km}$ and $c_{\text{IH}} = 200 \text{ ms}^{-1}$, while the NW-ward GWs would have intrinsic periods of 18 min, $\lambda_z = 52 \text{ km}$ and $c_{\text{IH}} = 76 \text{ ms}^{-1}$. Because λ_z was much larger for the SE-ward than NW-ward GWs, (1) z_{diss} would have been much larger for the SE-ward GWs, and (2) the GW amplitudes would have been much smaller for the NW-ward GWs [Vadas, 2007]. Because $c_{\text{IH}} > 100 \text{ ms}^{-1}$, the SE-ward GWs likely would have easily propagated to the 630.0 nm layer; whereas because $c_{\text{IH}} < 100 \text{ ms}^{-1}$ for the NW-ward GWs, they likely would not have propagated above $z = 150 \text{ km}$ because of molecular viscosity [Vadas, 2007]. For this larger NW wind, then, while the SE-ward GWs would have perturbed the 630.0 nm layer, the NW-ward GWs would have dissipated far below the layer. Figures 6 and 7 both show that the meridional wind increased in amplitude toward the NW direction from 8:00 to 12:00 UT due to the diurnal tide. From the above reasoning, we would then infer that the amplitudes of the SE-ward GWs should have grown during this time. In fact, this is what we see in Figure 2 where the 630.0 nm wave amplitude increased steadily from 4 R to 10 R (2.5–5%) during the period 9:30–11:00 UT.

[28] From the above arguments, we hypothesize that the background wind along the NW direction might have been $30\text{--}60 \text{ ms}^{-1}$ at $\sim 10:00 \text{ UT}$, enabling both the SE and

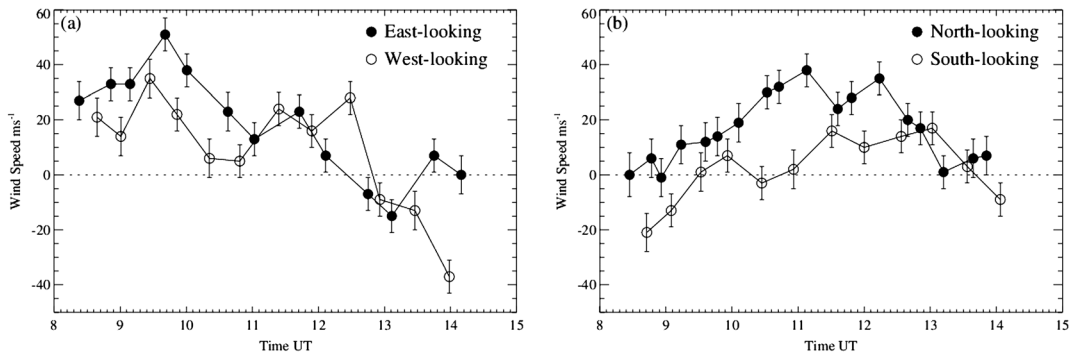


Figure 9. Neutral (a) zonal and (b) meridional OH winds obtained by the Fabry-Perot spectrometer at MJUO during the night of 4 March 2009.

NW-ward GWs to propagate to $z > 220$ km and perturb the 630.0 nm layer. However, after that time, the background wind in the NW direction likely increased, thereby decreasing (increasing) λ_z and c_{IH} for the NW (SE)-ward GWs. This would have enabled the SE-ward GWs to survive to even higher altitudes, thereby achieving larger amplitudes within the layer. However, this would also have caused the NW-ward GWs to dissipate at lower altitudes (below the layer). So, the weak signature and short time history of the NW-ward GWs as compared to the SW-ward GWs is consistent with the likely change in the background wind at $z = 250$ km that evening due to the diurnal tide.

3.2. Mesospheric Gravity Wave Activity

[29] Prior to and during the thermospheric wave activity, strong gravity wave activity was also observed at 85–95 km altitude region in the upper mesosphere. This consisted of two separate events in the OH, Na, and $O(^1S)$ emissions. The wave activity in $O(^1S)$ emission is shown in Figure 8 as a sequence of six HFP-filtered, unwarped images.

[30] At the start of observations (8:30 UT), a set of weak gravity waves was propagating due south (azimuth = 180°) in the three emissions. At the same time, another set of waves were propagating at an azimuth of 210° toward the southwest; however, they disappeared after about 10:30 UT. The southward-propagating gravity waves were initially weak but grew in amplitude until reaching a maximum at around 11:00 UT. They exhibited a marked nonsinusoidal, surge-like behavior and showed clear evidence of instability and breaking, particularly in the $O(^1S)$ emission. For example, small-scale instabilities, or ripples, formed during the passage of the MLT waves (shown clearly in Figures 8a–8f) and grew in amplitude as the amplitude of the gravity waves decreased. The phase fronts of the ripples were aligned obliquely to the propagation direction of the MLT waves.

[31] The OH and Na emission brightness variations due to their respective gravity waves were markedly less pronounced than observed in the $O(^1S)$ emission, which suggested that the wave-breaking process occurred at an altitude closest to the $O(^1S)$ emission layer, above the other two. The wavefronts associated with the southward-propagating gravity waves were also bent, with the eastern portions propagating toward the southeast (azimuth = 160°). The variation in propagation direction across the wavefronts is likely indicative of a spatially confined GW source, such

as wind flow over a few mountains (not an infinite chain of mountains). It may indicate the presence of a horizontal wind shear or temperature gradient that altered the propagation characteristics of the waves.

[32] The background zenith radiance of the 557.7 nm emission almost doubled between 10:00 and 11:00 UT, from 160 ± 8 R to 295 ± 11 R (see Figure 5). The enhancement was correlated with the passage of the large southward gravity waves in the 557.7 nm emission. The brightness decreased back to 165 ± 5 R after their passage, at 11:45 UT. In contrast, the OH and Na zenith emissions both showed a gradual decrease over the course of the MLT wave event.

[33] Horizontal neutral OH wind measurements were obtained during the night by the collocated FPS at Mt John [Hernandez and Smith, 1995]. These are shown in Figure 9. The FPS samples the nightglow at the four cardinal points at

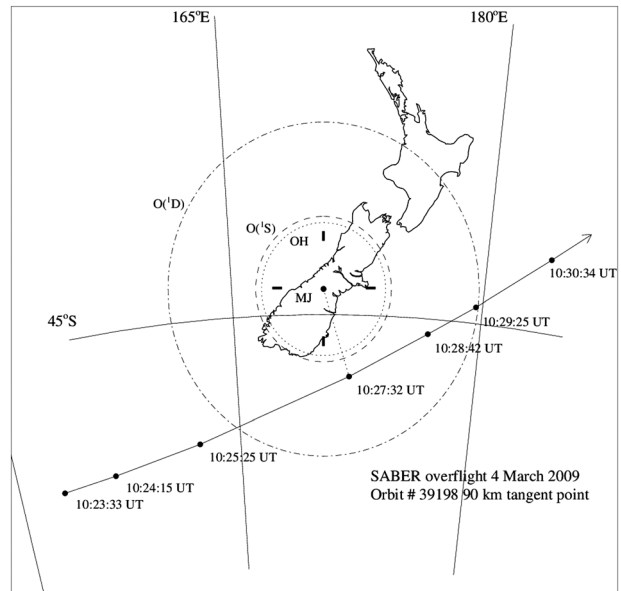


Figure 10. Location map showing the SABER-TIMED overpass trajectory over Mt. John (MJ) on 4 March 2009 at 10:23–10:31 UT. The sampling areas of the OH, $O(^1S)$, and $O(^1D)$ emissions down to 15° elevation are shown. Also shown, as bold bars, are the sampling regions of the FPS in the four cardinal directions.

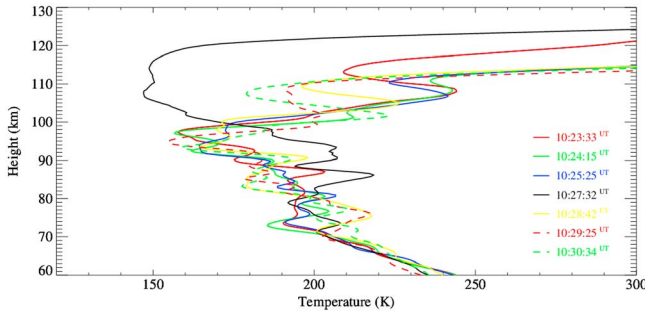


Figure 11. SABER temperature profiles obtained during an overpass of Mt. John Observatory on 4 March 2009 at the times shown in Figure 4. The profile at closest approach (black curve at 10:27:32 UT) stands out as unique among the profiles. It shows a region of heating at 90–100 km and a larger region of cooling between 105 and 120 km altitude, a condition consistent with overturning and mixing due to turbulence in the region as a result of gravity wave breaking.

20° elevation and at zenith in a cyclic sequence during the course of the night. The sampling points are shown in Figure 10 as four bold bars within the field of view of the imager. Oppositely sampled directions (N-S or E-W) are approximately 470 km apart.

[34] The FPS wind measurements exhibited variations of 15–40 ms^{-1} during the course of the night. Linear fits to the wind measurements shown in Figures 9a and 9b indicate that the zonal wind variation leads the meridional winds by about 2 h, which suggests that the wind field was dominated by an 8 h variation due to a large inertio-gravity wave or a terdiurnal tidal mode. The wind vectors rotated counter-clockwise during the course of the night, which is consistent with an upward-propagating gravity wave or tidal mode in this Southern Hemisphere location.

[35] Interestingly, horizontal wind gradients occurred between opposing look directions during the period of the MLT gravity wave activity (~8:00–12:00 UT) (Figures 9a and 9b). In particular, the meridional wind gradient reached a maximum at 11:00 UT, coinciding with the maximum amplitude of the southward MLT gravity waves in the images. At that time, the meridional wind was directed 35 ms^{-1} northward in the north-looking view and 0–5 ms^{-1} northward in the south-looking view (Figure 9b). This suggests that within the field of view, southward momentum was deposited within the MLT region, consistent with the breaking of southward-propagating GWs. We estimate a southward mean flow acceleration of 30 $\text{ms}^{-1} \text{h}^{-1}$ from 10:00 to 11:00 UT due to the GW breaking. This is much less than the reported acceleration which occurred because of a large wave-breaking event in the MLT [Fritts *et al.*, 2002]. Additionally, a zonal wind gradient of 20 ms^{-1} in the east- and west-looking views occurred prior to the maximum of the MLT waves but diminished thereafter (Figure 9a). The zenith wind measurements indicated the presence of a 2 h variation in the vertical wind during the night superimposed upon the larger 8 h variation. The gradual decrease in the OH zenith brightness during the course of the night and seen with the imager was also seen in the FPS measurements.

[36] Further evidence of the wave-breaking activity observed in the MLT images was provided by the Sounding of the Atmosphere using Broadband Emission Radiometry (SABER) instrument temperature profiles. The NASA TIMED satellite passed within 410 km of the Mt. John site during the period of the wave activity (Figure 10), and the onboard SABER instrument obtained OH emission and temperature profiles (Figure 11). Most of the profiles show a region of 30–40 K cooling at 90–100 km, but the profile obtained at closest approach is warmer than the others by 25–30 K. Closest approach occurred near 10:28 UT (between Figures 8d and 8e), and the corresponding temperature profile, shown in Figure 11 (black curve), reveals a significant region of cooling, 50 to 70 K cooler than the surrounding profiles, over the 100–120 km altitude region. The altitude of the mesopause had also effectively increased by 15 km from around 95 km to near 110 km. Note that GW breaking is associated with cooling above heating, depending on the turbulent Prandtl number and the localization of the breaking region [Walterscheid, 1981; Liu, 2000].

[37] In addition, the profile obtained at closest approach is consistent with a large gravity wave-breaking process occurring at the 90–100 km altitude level that caused local heating via turbulent diffusion. The result of wave breaking was to cause a region 25–30 K warmer than the surrounding profiles. The large region of cooling at 100–110 km is due to wave advection of heat as the wave breaks and advects air downward. The closest approach profile also appears to be highly localized to within an area of <400 km since the two next closest temperature profiles do not show any evidence of strong cooling at that altitude region. The horizontal scale size of the cooling region is twice the approximate width of New Zealand and is similar to that of a MLT temperature inversion associated with a gravity wave bore disturbance over Arecibo and observed with SABER and a ground-based lidar (~500 km) [Smith *et al.*, 2005].

[38] The SABER overpass provided vertical profiles of the OH volume emission rate and yielded a mean height of 87.3 km ($\sigma=1.6$ km) for the OH layer with a FWHM thickness of 8.3 km ($\sigma=0.8$ km). The OH layer emission profile at closest approach was the lowest and broadest of the seven profiles, 85.0 km with a FWHM thickness of 9.5 km, which is also consistent with a gravity wave-breaking event, in which downward vertical advection occurs in conjunction with turbulent diffusion which broadens the layer. Also, by comparing the phase differences of the MLT gravity waves in the OH, Na, and O(¹S) emissions, the median vertical wavelength of MLT waves during 9:00–12:00 UT was 17 ± 5 km, which is consistent with wave structures seen in the SABER temperature profiles in the 80 to 100 km altitude region (Figure 11).

4. Modeling the Secondary Gravity Waves in the Thermosphere

[39] GWs are excited by the wind flow over mountains [Fritts and Alexander, 2003]. These waves are called “mountain waves.” From Figure 1, the altitude of the mountain ranges on both islands of New Zealand is 1000–3000 m. Figure 12 shows the wind at ~1500 m at 0:00 and 12:00 UT on 4 March 2009. The winds over the South Island are south and southeastward with speeds of

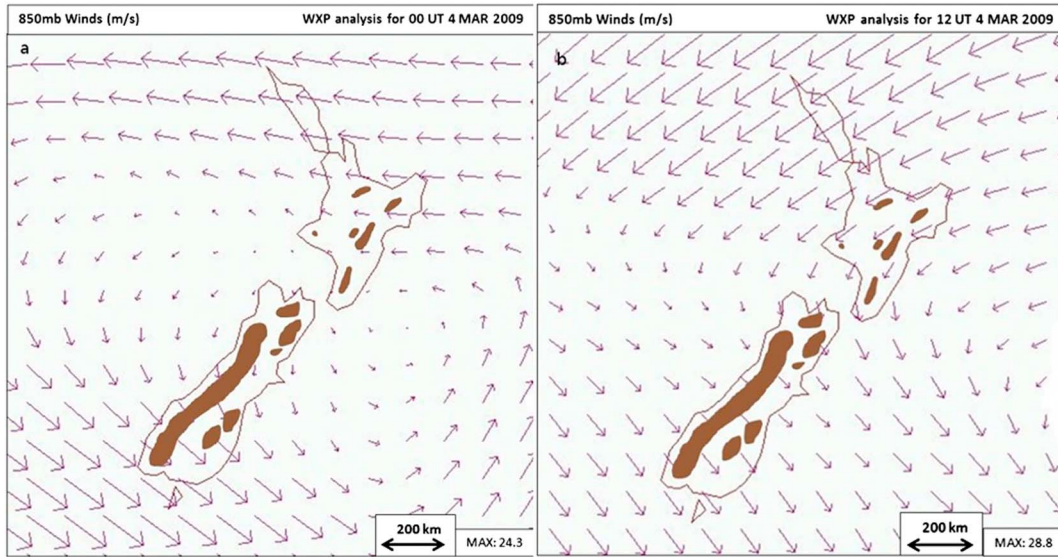


Figure 12. Vector winds (purple arrows) in ms^{-1} at 850 mb (corresponding to ~ 1500 m) at (a) 0:00 UT and (b) 12:00 UT over New Zealand (WXP analysis, Plymouth State). The vector lengths are proportional to the speed, which have maximum values of 24.3 and 28.8 ms^{-1} , respectively. Brown shading shows the approximate regions where the mountains are taller than 1000 m.

10–20 ms^{-1} , while the winds over the North Island are westward and southwestward with smaller speeds of 5–15 ms^{-1} . We estimate the nondimensional mountain height to be $hN/U_H \sim 2-3$, a value that is associated with significant mountain-wave generation [Vadas and Nicolls, 2009]. A degree of nonlinearity is probably also present. Here h is the mountain height (2000–3000 m), $N \sim 0.02 \text{ rad s}^{-1}$ (Brunt-Vaisala frequency), and U_H is the wind speed. GW amplitudes grow exponentially with altitude in the lower atmosphere, thereby allowing mountain waves with initially linear amplitudes to become nonlinear and break in the mesosphere. Thus, Figure 12 shows that it is quite likely

that mountain waves were created and broke in the MLT region this evening.

[40] Figure 13 shows tropospheric wind measurements, in the form of hodographs, obtained from three radiosonde flights in New Zealand (see Figure 1 for locations): two originating from Hokitika at 00:00 UT and at 12:00 UT and one from Christchurch at 06:00 UT. With regard to the prevailing winds, Hokitika is located on the windward side of the Southern Alps and Christchurch on the leeward side. The Hokitika measurements in Figures 13a and 13b show a southeastward wind flow of 5–10 ms^{-1} perpendicular to the axis of the South Island up to 4–5 km altitude.

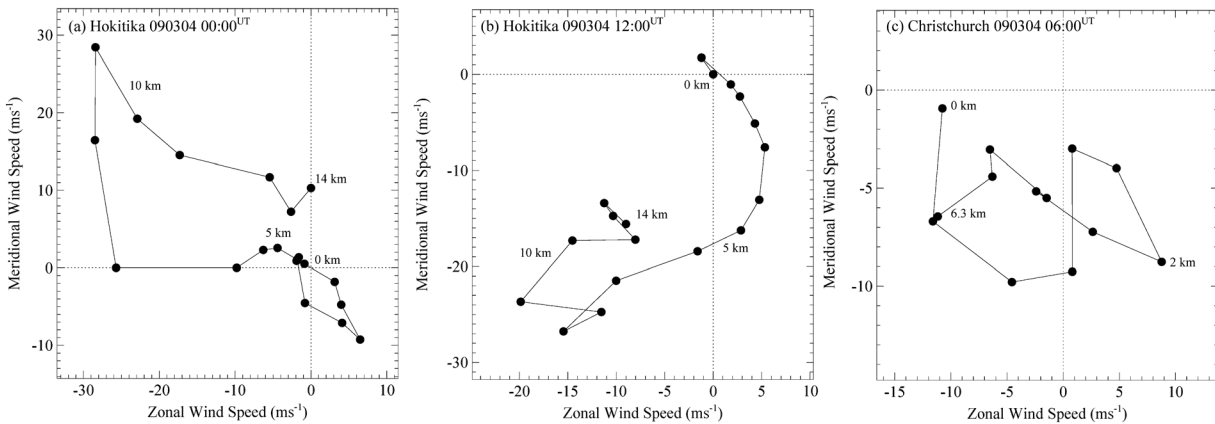


Figure 13. Neutral wind measurements obtained from three radiosonde flights launched from (a and b) Hokitika and (c) Christchurch on 4 March 2009 (see Figure 1 for locations). These are measurements made by the New Zealand Meteorological Service. The horizontal and vertical axes represent the zonal and meridional winds directions, respectively. The Hokitika measurements show a SE-ward wind flow at low altitudes followed by a stronger NW-ward wind flow above 4 km. The Christchurch measurements show a large gravity wave structure with general southward wind flow at all levels.

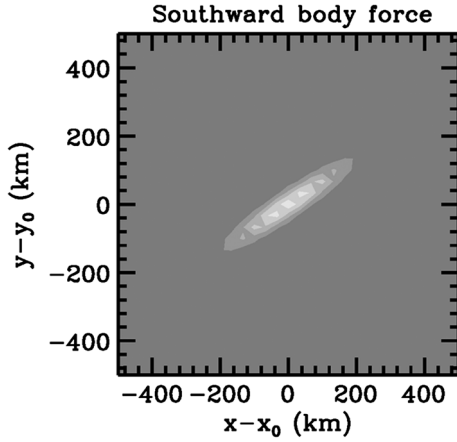


Figure 14. Horizontal slice of the southward body force at $z = 100$ km. This force is aligned in the direction of the largest mountains in the southern island of New Zealand.

Above that level, a strong northwestward (0:00 UT) or southwestward (12:00 UT) flow is seen. The Christchurch winds at 6:00 UT (Figure 13c) show a large gravity wave structure in the lower troposphere winds modulating a predominantly southward flow of $5\text{--}10\text{ ms}^{-1}$. Using the Christchurch radiosonde wind measurements and $N = 0.012$ for a typical troposphere, we estimate $\lambda_z (= 2\pi U_H/N)$ for the tropospheric gravity wave to be $3\text{--}5$ km, which agrees well with estimates made from Figure 13c of $\lambda_z = 3\text{--}6$ km.

[41] We can therefore assume that the southward-breaking GWs in Figure 8 are mountain waves, created by southward air flow over the Southern Alps on the south island of New Zealand (see Figures 12 and 13). Furthermore, we assume that this wind is uniform. This would create mountain waves with similar amplitudes, causing them to break at similar altitudes in the MLT. Upon breaking, momentum is deposited in localized regions in space and time, creating multiple accelerations or body forces in the direction of wave propagation [Fritts *et al.*, 2006]. Because these body forces act in the same direction (since the mountain range alignment is approximately linear and the wind is assumed constant), the body forces add together coherently, thereby creating a large body force with a geometry similar to the ridgeline of the mountain range. Because the breaking GWs are propagating approximately southward (see Figure 8), this body force is approximately southward.

[42] We wish to understand the basic properties of the excited secondary GWs. Therefore, we represent this body force as a simple Gaussian function in space. This function has a total width of $D_x = 4.5 \sigma_x = 100$ km and a length of $D_y = 4.5 \sigma_y = 600$ km (representative of the south island). We center the body force at $z_0 = 100$ km, because the wave breaking is strongest at the 557.7 nm emission. Although the azimuth of the southern island is 45° , the azimuth of the Alpine Fault (which defines the mountain spine on the south island) is $\sim 56^\circ$. We therefore choose the body force to be oriented at an azimuthal angle of 56° . The total depth, D_z , is given by the vertical wavelength of

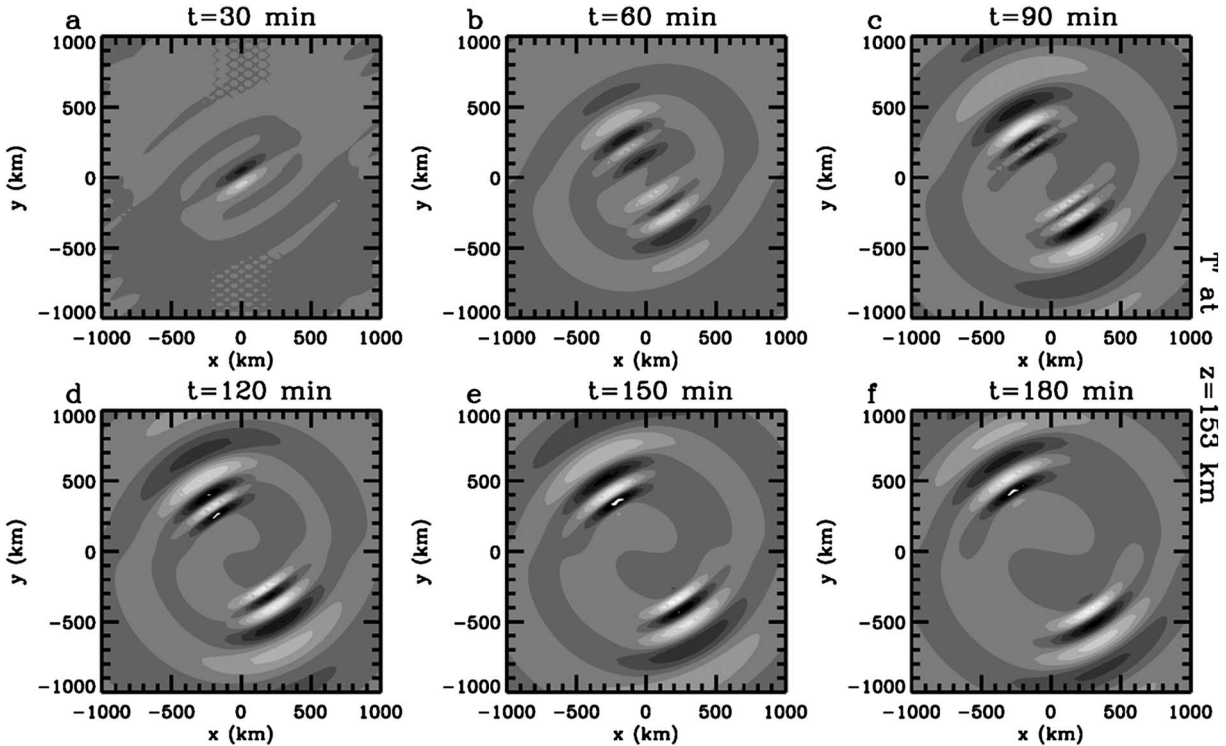


Figure 15. Horizontal slice of the temperature perturbations of the secondary GWs at $z = 153$ km excited by the body force shown in Figure 14. (a) $t = 30$ min, (b) $t = 60$ min, (c) $t = 90$ min, (d) $t = 120$ min, (e) $t = 150$ min, and (f) $t = 180$ min. Light (dark) colors denote positive (negative) values, in 2 K intervals. The maximum perturbation amplitude is 12 K.

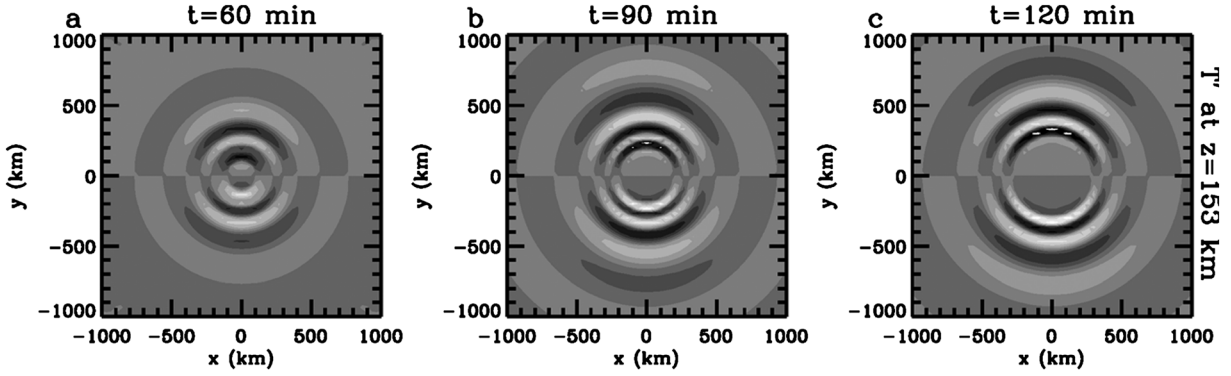


Figure 16. Horizontal slice of the temperature perturbations of the secondary GWs at $z = 150$ km excited by a circular body force with $D_x = D_y$. (a) $t = 60$ min, (b) 90 min, and (c) 120 min. Light (dark) colors denote positive (negative) values, in 0.6 K intervals. The maximum perturbation amplitude is 3.5 K.

the MLT GWs: thus, we set $D_z = 4.5$ $\sigma_z = 17$ km (see Table 1). The force duration is approximately the wave period: thus, we set $\chi = 30$ min (see Table 1). We choose an amplitude of $v_0 = 30$ ms^{-1} from Figure 9. The functional form of the southward body force is then as follows :

$$F_y = v_0 \exp\left(-\frac{(x' - x_0)^2}{2\sigma_x^2} - \frac{(y' - y_0)^2}{2\sigma_y^2} - \frac{(z - z_0)^2}{2\sigma_z^2}\right) F(t), \quad (2)$$

where (x_0, y_0) is the center of the force, $a = 2\pi/\chi$ is the forcing frequency, and

$$F(t) = (1/\chi) (1 - \cos(at)) \text{ for } 0 < t < \chi, \\ = 0 \text{ otherwise.}$$

[43] Here, x' and y' are the zonal and meridional coordinates in the rotated reference frame:

$$x' = x \cos(\phi) + y \sin(\phi) \\ y' = -x \sin(\phi) + y \cos(\phi),$$

where ϕ is the angle counterclockwise from east, $\phi = 90^\circ - 56^\circ = 34^\circ$. Figure 14 shows the geometry of this southward force F_y .

[44] We now calculate the spectrum of secondary GWs excited by this body force. Because the force depth is greater than the density scale height ($H \sim 7$ km), we cannot accurately calculate the excited secondary GW spectrum using the Boussinesq solutions from *Vadas and Fritts [2001]* [see *Vadas, 2013*]. Instead, we must use the compressible solutions recently derived in *Vadas [2013]*. These solutions are solved in a windless, isothermal, dissipative-less environment. Figure 15 shows the temperature perturbations of the secondary GWs excited by this body force at $z = 150$ km using these solutions. The secondary GWs have nearly linear phase fronts that are parallel to the Southern Alps. However, some curvature in the fronts is noticeable. This occurs because of the finite length of the mountain range. Such features mimic the observations in Figure 2. Additionally, note that the horizontal wavelengths of the GWs increase as the distance perpendicular to the Southern Alps increases. This feature is also easily noticeable in the 630.0 nm observations shown in Figure 2, especially at 10:43 and 10:52 UT.

[45] We now contrast these results with those for a single, southward Gaussian body force with $D_x = D_y = 100$ km. All other parameters are the same as in Figure 15. Figure 16 shows the temperature perturbations of the secondary GWs excited by this force at $z = 150$ km. In contrast to Figure 15, these secondary GWs have curved phase fronts that are antisymmetric about the y axis. However, they also display an increasing horizontal wavelength with distance from the force, similar to Figure 15.

5. Discussion

[46] The particular morphology of the observed 630.0 nm waves has not been reported previously in all-sky imagery. Thermospheric wave phenomena, such as MSTIDs for example, tend to be less well defined visually in all-sky images. Furthermore, the observation of two sets of waves originating simultaneously and propagating in opposite directions from a single region is unusual. Using the model results from this paper, we suggest that the 630.0 nm GWs reported here were generated simultaneously in the lower thermosphere at $z \sim 100$ – 110 km from GW breaking occurring in the MLT above the Southern Alps in New Zealand. The waves then propagated SE- and NW-ward up into the thermosphere, where they modulated the 630.0 nm emission. Because the background wind was likely NW-ward, those GWs propagating NW-ward had decreasing vertical wavelengths and therefore smaller amplitudes (due to damping by molecular viscosity) than those propagating SE-ward. Because a spectrum of GWs is excited, the signal in the 630.0 nm emission will last for hours for each body forcing.

[47] The vertical wavelength of the SE-ward thermospheric waves was likely large compared to the width of the 630.0 nm emission layer (FWHM ~ 50 km), so any potential to cause a ‘‘Venetian blind effect’’ was minimal. This effect can be caused by the combination of the integrating nature of the all-sky imaging technique and the viewing angle change as a gravity wave train propagates across the sky. Since a GW has tilted wavefronts, the wave pattern may be visible on only one side of the field of view where the wave field is sampled up through the tilted phase fronts.

[48] During the period of the observed wave activity, 5 min ionograms were obtained between 8:00 and 12:00 UT

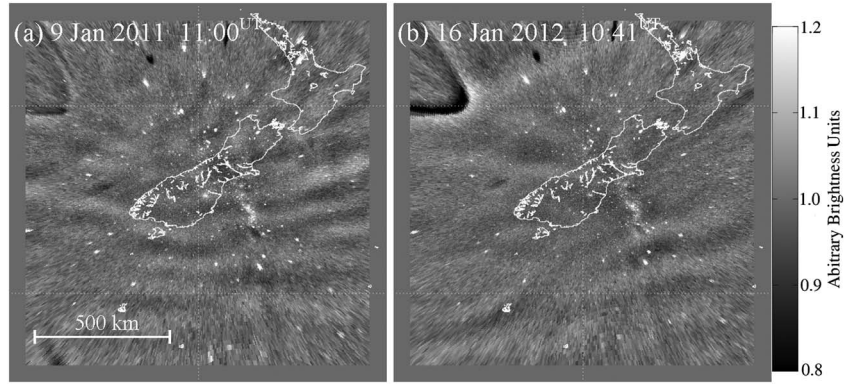


Figure 17. Unwarped 630.0 nm all-sky images of two thermospheric wave events similar to the one described in the present study. Both events were observed in the southeastern quadrant propagating southeastward away from Mt John. Neither event was observed in the northwestern quadrant, suggesting that the waves were generated to the southeast of Mt John.

by the University of Canterbury ionosonde [Smith and Baggaley, 1991] (http://www.ips.gov.au/HF_Systems/1/3) (figure not shown). The ionosonde is located at Eyrewell, approximately 170 km NE of MJUO. The traces were initially narrow and well defined, and they exhibited double F region traces due to ground-layer reflection, which indicated that the thermosphere was essentially horizontal with little or no tilting of the ionospheric layers. After $\sim 9:30$ UT, the traces broadened and spread in virtual altitude, a feature which can be indicative of unresolved scattering structures, such as waves and turbulence, within the ambient ionization above 100 km altitude. The horizontal resolution of ionosondes is generally low so the observed spreading is consistent with gravity wave activity and/or turbulent diffusion. Large-scale dynamical structures and tilted gravity wave structures in the ionosphere tend to cause kinks along the ionogram traces, which were not observed.

[49] Observations of the generation of secondary GWs in the MLT and above are scarce. Vadas and Nicolls [2009] recorded coherent gravity wave structures with horizontal scale sizes of 350–450 km and periods of 20–24 min in the lower thermosphere at 150–300 km altitude using the Poker Flat Incoherent Scatter Radar at Poker Flat, Alaska. Their analysis suggested that the waves were secondary GWs that had been generated from the breaking of mountain waves that had, in turn, originated from lower in the atmosphere (troposphere) due to orographic forcing. Vadas *et al.* [2003] and Vadas [2013] discussed the theory of the generation of medium-scale secondary gravity waves in the lower atmosphere and thermosphere.

[50] The orientation of the thermospheric waves shown in Figure 2 appear to be associated with the New Zealand landmass. The landmass, particularly the South Island, presents a large barrier to the prevailing westerly winds over the Southern Ocean. The direction of wave propagation is slightly southward of the locus of 1000 m altitude elevation contours shown in Figure 1. Thus, the curvature associated with the thermospheric wavefronts can be attributed to the localized region of forcing presented by the New Zealand landmass. Wave events in the 630.0 nm emission showing similar behavior have been seen at Mt John at other times (see Figure 17). In these images, only the SE-ward propagating

waves are visible; however, they appear to originate above New Zealand (i.e., are only visible in the SE quadrant of the images), similar to the case studied in this paper. Dissipative filtering of the waves in the thermosphere, and the influence of the background wind on their propagation, is likely responsible for the appearance of only the SE-ward waves in these images. The background wind at $z=250$ km is dominated by the diurnal tide at this latitude. This wind is NW-ward after $\sim 10:00$ UT (see Figure 7), although there is likely some day-to-day variability in this time. The amplitude of the tide experiences day-to-day variability. As shown in section 3.1, a stronger NW-ward wind (of $\sim 100 \text{ ms}^{-1}$) would allow the SE-ward waves to propagate to $z \sim 250$ km; however, it would shorten the vertical wavelengths of the NW-ward waves, causing them to dissipate from molecular viscosity below the 630.0 nm emission layer. The fact that the 630.0 nm waves in Figure 17 are seen only in the SE quadrant of these images supports the hypothesis that the formation of these waves is associated with the New Zealand landmass.

6. Summary

[51] Oppositely propagating gravity waves (GWs) were observed in thermospheric 630.0 nm emission all-sky images at $z \sim 250$ km altitude at the Mt. John Observatory, New Zealand. These waves propagated away from the New Zealand landmass, suggesting a common origin associated with the landmass. Additionally, the wavefronts were aligned parallel to the axis of the Southern Alps in the South Island of New Zealand, suggesting that orographic forcing played a part in their formation. At the same time and location, large GW breaking events were seen in the MLT. We note that the South Island of New Zealand is known for causing orographic effects in the mesosphere, particularly during the winter months [e.g., Jiang *et al.*, 2005].

[52] From balloon soundings, we showed that mountain wave generation above the Southern Alps was quite likely that day. We then modeled the medium-scale secondary GWs excited by body forces created by the breaking of mountain waves in the MLT. We found that these waves have similar propagation directions, morphology,

and horizontal wavelengths as those seen in the 630.0 nm images. Therefore, it is likely that the observed thermospheric 630.0 nm GWs were secondary GWs generated from mountain wave breaking in the MLT. Animations of the 630.0 nm and 557.7 nm wave events during the night can be viewed in the supplementary materials section.

[53] **Acknowledgments.** This project was funded by a NSF CEDAR grant ATM#0640780. S.M.S. is grateful to Messrs. Alan Gilmore and Graeme Plank at the University of Canterbury for their continued support of the imager operations at MJUO. Thanks also to Prof. Andrew Sturman for providing the contour map of New Zealand and to Drs. J.M. Russell and M.G. Mlynczak, Mr. L.L. Gordley, and the rest of the SABER Team at GATS Inc. for the use of the SABER emission data. J.M.R. and M.G. M. are supported in part by the NASA Science Mission Directorate and the Langley NASA Science Directorate. S.L.V. was supported by NSF Grant AGS-1139149 and NASA Contract NNH12CE58C. S.L.V. would like to thank Patrice Sutter for Figure 12 and Ben Foster for the TIME-GCM data. The neutral wind measurements are supported by ATM-0639718 to the University of Washington.

[54] Robert Lysak thanks Gary R. Swenson and another reviewer for their assistance in evaluating this paper.

References

- Burnside, R. G., J. W. Meriwether, and M. R. Torr (1977), Contamination of ground-based measurements of OI (6300 Å) and NI (5200 Å) airglow by OH emissions, *Planet. Space Sci.*, 25(10), 985–988.
- Evans, W. F. J., R. L. Gattinger, T. G. Slanger, D. V. Saran, D. A. Degenstein, and E. J. Llewellyn (2010), Discovery of the FeO orange bands in the terrestrial night airglow spectrum obtained with OSIRIS on the Odin spacecraft, *Geophys. Res. Lett.*, 37, L22105, doi:10.1029/2010GL045310.
- Forbes, J. M., X. Zhang, S. Palo, J. Russell, C. J. Mertens, and M. Mlynczak (2008), Tidal variability in the ionospheric dynamo region, *J. Geophys. Res.*, 113, A02310, doi:10.1029/2007JA012737.
- Fritts, D. C., and M. J. Alexander (2003), Gravity wave dynamics and effects in the middle atmosphere, *Rev. Geophys.*, 41(1), 1003, doi:10.1029/2001RG000106.
- Fritts, D. C., S. L. Vadas, and Y. Yamada (2002), An estimate of strong local body forcing and gravity wave radiation based on OH airglow and meteor radar observations, *Geophys. Res. Lett.*, 29(10), 1429, doi:10.1029/2001GL013753.
- Fritts, D. C., S. L. Vadas, K. Wan, and J. A. Werne (2006), Mean and variable forcing of the middle atmosphere by gravity waves, *J. Atmos. Sol. Terr. Phys.*, 68, 247–265.
- Fritts, D. C., and T. Lund (2011), Gravity wave influences in the thermosphere and ionosphere: Observations and recent modeling, in *Aeronomy of the Earth's Atmosphere and Ionosphere*, edited by M. A. Abdu, D. Pancheva, and A. Bhattacharyya, pp. 109–130, IAGA Special Sopron Book Series Vol. 2, Springer, Dordrecht.
- Fritts, D. C., and S. L. Vadas (2008), Gravity wave penetration into the thermosphere: Sensitivity to solar cycle variations and mean winds, *Ann. Geophys.*, 26, 3841–3861.
- Kelley, M. C., and J. J. Makela (2001), Resolution of the discrepancy between experiment and theory of midlatitude F-region structures, *Geophys. Res. Lett.*, 28, 2589–2592.
- Hays, P., and S. K. Atreya (1971), The influence of thermospheric winds on the auroral red-line profiles of atomic oxygen, *Planet. Space Sci.*, 19, 1225–1228.
- Hernandez, G. (1972), Determination of the quenching of O(¹D) by molecular nitrogen using the Ionospheric Modification Experiment, *J. Geophys. Res.*, 77, 3625–3629.
- Hernandez, G. (1974), Contamination of the OI(³P₂–¹D₂) emission line by the (9–3) band of OH X²II in high-resolution measurements of the night sky, *J. Geophys. Res.*, 79, 1119–1123.
- Hernandez, G. R. W. Smith (1995), Winds and vertical wavelengths deduced from the ground-based measurement the Doppler shifts of the O₂(b ¹Σ_g⁺ – K _{3Σ_g⁻), OI(¹D₂ – ¹S₀), and the K ²Π OH (⁶⁻²) band P₁₍₂₎ c,d line emissions in the midlatitude upper middle atmosphere, *J. Geophys. Res. Lett.*, 22(4), 369–372.}
- Jiang, J. H., D. L. Wu, S. D. Eckermann, and J. Ma (2003), Mountain waves in the middle atmosphere: Microwave limb sounder observations and analyses, *Adv. Space Res.*, 32(5), 801–806.
- Jiang, J. H., S. D. Eckermann, D. L. Wu, K. Hocke, B. Wang, J. Ma, and Y. Zhang (2005), Seasonal variation of gravity wave sources from satellite observation, *Adv. Space Res.*, 35(11), 1925–1932.
- Lane, T. P., M. J. Reeder, B. R. Morton, and T. L. Clark (2000), Observations and numerical modelling of mountain waves over the southern alps of New Zealand, *Q. J. R. Meteorol. Soc.*, 126, 2765–2788.
- Liu, H.-L. (2000), Temperature changes due to gravity wave saturation, *J. Geophys. Res.*, 105, 12,329–12,336.
- Martinis, C., J. Baumgardner, J. Wroten, and M. Mendillo (2010), Seasonal dependence of MSTIDs obtained from 630.0 nm airglow imaging at Arecibo, *Geophys. Res. Lett.*, 37, L11103, doi:10.1029/2010GL043569.
- Osterbrock, D. E., J. P. Fulbright, A. R. Martel, M. J. Keane, S. C. Trager, and G. Basri (1996), Night-sky high-resolution spectral atlas of OH and O₂ emission lines for echelle spectrograph wavelength calibration, *Pub. Astro. Soc. Pac.*, 108, 277–306.
- Roble, R. G., and E. C. Ridley (1994), A Thermosphere-Ionosphere-Mesosphere-Electrodynamics General Circulation Model (TIME-GCM): Equinox solar cycle minimum simulations (30–500 km), *Geophys. Res. Lett.*, 21, 417–420.
- Saito, A., M. Nishimura, M. Yamamoto, S. Fukao, T. Tsugawa, Y. Otsuka, S. Miyazaki, and M. C. Kelley (2002), Observations of traveling ionospheric disturbances and 3-m scale irregularities in the nighttime F-region ionosphere with the MU radar and a GPS network, *Earth Planet. Space*, 54, 31–44.
- Saran, D. V., T. G. Slanger, W. Feng, and J. M. C. Plane (2011), FeO emission in the mesosphere: Detectability, diurnal behavior, and modeling, *J. Geophys. Res.*, 116, D12303, doi:10.1029/2011JD015662.
- Shiokawa, K., C. Ihara, Y. Otsuka, and T. Ogawa (2003), Statistical study of nighttime medium-scale traveling ionospheric disturbances using midlatitude airglow images, *J. Geophys. Res.*, 108(A1), 1052, doi:10.1029/2002JA009491.
- Smith, S. M., and W. J. Baggaley (1991), Horizontal motions of south temperate zone sporadic-E using an ionosonde array, *Planet. Space Sci.*, 39(7), 1007–1015.
- Smith, S. M., J. Friedman, S. Raizada, C. Tepley, J. Baumgardner, and M. Mendillo (2005), Evidence of mesospheric bore formation from a breaking gravity wave event: Simultaneous imaging and lidar measurements, *J. Atmos. Sol. Terr. Phys.*, 67(4), 345–356, doi:10.1016/j.jastp.2004.11.008.
- Smith, S. M., J. Baumgardner, and M. Mendillo (2009), Evidence of mesospheric gravity-waves generated by orographic forcing in the troposphere, *Geophys. Res. Lett.*, 36, L08807, doi:10.1029/2008GL036936.
- Vadas, S. L., and D. C. Fritts (2001), Gravity wave radiation and mean responses to local body forces in the atmosphere, *J. Atmos. Sci.*, 58, 2249–2279.
- Vadas, S. L. (2007), Horizontal and vertical propagation and dissipation of gravity waves in the thermosphere from lower atmospheric and thermospheric sources, *J. Geophys. Res.*, 112, A06305, doi:10.1029/2006JA011845.
- Vadas, S. L., and M. J. Nicolls (2009), Temporal evolution of neutral, thermospheric winds and plasma response using PFISR measurements of gravity waves, *J. Atmos. Sol. Terr. Phys.*, 71, 744–770.
- Vadas, S. L., and H.-L. Liu (2009), The generation of large-scale gravity waves and neutral winds in the thermosphere from the dissipation of convectively-generated gravity waves, *J. Geophys. Res.*, 114, A10310, doi:10.1029/2009JA014108.
- Vadas, S. L., D. C. Fritts, and M. J. Alexander (2003), Mechanism for the generation of secondary waves in wave breaking regions, *J. Atmos. Sci.*, 60, 194–214.
- Vadas, S. L., and H.-L. Liu (2013), Numerical modeling of the large-scale neutral and plasma responses to the body forces created by the dissipation of gravity waves from 6 h of deep convection in Brazil, *J. Geophys. Res.*, 108, doi:10.1002/jgra.5249.
- Vadas, S. L. (2013), Compressible f-plane solutions to body forces, heatings, and coolings, and application to the primary and secondary gravity waves generated by a deep convective plume, *J. Geophys. Res.*, 118, doi:10.1002/jgra.50163.
- Walterscheid, R. L. (1981), Dynamical cooling induced by dissipating internal gravity-waves, *J. Geophys. Res.*, 8, 1235–1238.
- Wu, D. L. (2004), Mesoscale gravity wave variances from AMSU-A radiances, *Geophys. Res. Lett.*, 31, L12114, doi:10.1029/2004GL019562.
- Wu, D. L., P. Preusse, S. D. Eckermann, J. H. Jiang, M. de la Torre Juarez, L. Coy, and D. Y. Wang (2006), Remote sounding of atmospheric gravity waves with satellite limb and nadir techniques, *Adv. Space Res.*, 37, 2269–2277.